Crystalline and magnetic properties of CoO nanoparticles locally investigated by using radioactive indium tracer

Renata Santos
Programa de Pós-Graduação em Ciência e Engenharia de Materiais – PPGCEM- Universidade Federal do Pará,
Gabriel Cabrera-Pasca
Programa de Pós-Graduação em Ciência e Engenharia de Materiais – PPGCEM- Universidade Federal do Pará,
Cledilane Costa
Faculdade de Ciências Exatas e Tecnologia, Universidade Federal do Pará
Brianna Santos
Instituto de Pesquisas Energéticas e Nucleares, IPEN-CNEN/SP
Larissa Otubo
Instituto de Pesquisas Energéticas e Nucleares, IPEN-CNEN/SP
Luciano Pereira
Instituto de Pesquisas Energéticas e Nucleares, IPEN-CNEN/SP
Bruno Correa
Instituto de Pesquisas Energéticas e Nucleares, IPEN-CNEN/SP
Fernando Effenberger
Instituto de Pesquisas Energéticas e Nucleares, IPEN-CNEN/SP
Anastasia Burimova
Instituto de Pesquisas Energéticas e Nucleares, IPEN-CNEN/SP
Rafael Freitas
Instituto de Física da Universidade de São Paulo
Artur Carbonari (carbonar@ipen.br)
Instituto de Pesquisas Energéticas e Nucleares, IPEN-CNEN/SP

Research Article

Keywords: TEM, X-ray diffraction (XRD), perturbed angular correlations (PAC), ZFC-FC, magnetic nanoparticles (NPs)

Posted Date: July 8th, 2021

DOI: https://doi.org/10.21203/rs.3.rs-679601/v1

Crystalline and magnetic properties of CoO nanoparticles locally investigated by using radioactive indium tracer

Renata V. Santos[1], Gabriel A. Cabrera-Pasca[1,2], Cleidilane O. S. Costa[1,2], Brianna Bosch-Santos[3], Larissa Otubo[3], Luciano F. D. Pereira[3], Bruno S. Correa[3], Fernando B. Effenberger[3], Anastasia Burimova[3], Rafael S. Freitas[4], and Artur W. Carbonari[3,*]

[1]Programa de Pós-Graduação em Ciência e Engenharia de Materiais – PPGCEM- Universidade Federal do Pará, 67130-660 Ananindeua, PA, Brazil
[2]Faculdade de Ciências Exatas e Tecnologia, Universidade Federal do Pará, 68440-000 Abaetetuba, PA, Brazil
[3]Instituto de Pesquisas Energéticas e Nucleares, IPEN-CNEN/SP, 05508-000 São Paulo, SP, Brazil
[4]Instituto de Física, Universidade de São Paulo, 05508-090 São Paulo, SP, Brazil
[*]carbonar@ipen.br
[+]these authors contributed equally to this work

ABSTRACT

We herein report a comprehensive investigation on the magnetic, structural, and electric properties of CoO nanoparticles with different sizes by local inspection through hyperfine interactions measured in a wide range of temperatures (10-670 K) by using radioactive ^{111}In(^{111}Cd) tracers with the perturbed angular correlations (PAC) technique. Small cobalt oxide nanoparticles with 6.5 nm have been prepared by the wet chemical route, which has shown essential to incorporate radioactivity tracers during nucleation and grown syntheses. Nanocrystalline samples with 22 nm size were obtained by thermal treatments under low pressure of helium at 670 K. The hyperfine data were correlated with X-ray diffraction (XRD), ZFC-FC magnetic measurements and transmission electron microscopy (TEM) to describe the structure, magnetic properties, size, and shape of samples. An analysis of the temperature evolution of hyperfine parameters revealed that the structural distortion and the magnetic disorder in the core and on the surface layer play an important role in the magnetic behavior of CoO nanoparticles.

Introduction

Due to their great potential for application in new technological devices, magnetic nanoparticles (NPs) have captured the attention of researchers in several areas of scientific knowledge, and are being studied with increasing interest, promoting mainly the investigation of new synthesis routes and characterization methodology with the purpose to improve their performance[1–3]. For example, magnetic NPs can be applied in the production of ferrofluids, biosensors, battery materials, catalysts, drug delivery, magnetic resonance contrast agents, etc.[3–7]. All these applications are possible because NPs have shown a chemical stability and an enhancement of their magnetic properties. Particularly, NPs of magnetic transition metals are interesting because they present unique physical properties at the nanometric scales that differ drastically when compared to those of large particles[8–10].

The area/volume ratio is large in NPs and increases when their size decreases enhancing the influence of surface layer on their physical properties. Therefore, local techniques sensitive to different regions within an atomic scale are necessary to perform a detailed investigation and characterization of NPs[11,13,14,57]. The better understanding of local correlations will allow the development of new technological applications.

In order to have an adequate magnetic characterization of magnetic NPs it is necessary the knowledge of the magnetic structure, the transition temperature and the possible formations of crystalline or amorphous phases in NPs because these properties play an important role in the occurrence or not of magnetism. Regarding the magnetic phase transitions of nanoparticles, blocking temperature (T_B) often hinders the determination of the ordering temperature. T_B is a signature of the particle size reduction, typically extracted from the zero field cooling and field cooling (ZFC-FC) curves of magnetic measurements, with timescale around milliseconds (ms).

There is a probability that the magnetization of small magnetic NPs flip and reverse its direction at a certain temperature. The mean time between two flips is called the Néel relaxation time (τ_N). Considering that the magnetization in a magnetic nanoparticle is measured with a measurement time τ_m, then if in one experiment $\tau_m \gg\gg \tau_N$, the nanoparticle magnetization will flip several times during the measurement and the measured magnetization will average to zero. On the other hand, if in

another experiment $\tau_m \lll \tau_N$, the magnetization will not flip during the measurement, and the measured magnetization will be what the instantaneous magnetization was at the beginning of the measurement. The first experiment indicates that the nanoparticle would be in the superparamagnetic state, whereas in the second experiment it will be blocked in its initial state. Therefore, the state of the nanoparticle (superparamagnetic or blocked) depends on the measurement time that is a characteristics of each experimental technique. A transition between superparamagnetism and blocked state occurs when $\tau_m = \tau_N$,[15–17].

Hence, to inspect the ordering temperature in magnetic nanoparticles would be ideal to use an experimental technique with a timescale around nanosecond much smaller than AC susceptibility with a timescale around milliseconds. Hyperfine interaction techniques are suitable to accurately determine the temperature transitions and also allow characterizing short-range magnetic interactions by presenting this specific characteristic[14,18]. In addition, the local techniques are very efficient, because it can also determine the crystallinity, spurious phases, and local crystal distortions which sometimes are imperceptible by X-ray diffraction since the particles are very small.

The perturbed angular correlation (PAC) spectroscopy is a non-resonance hyperfine interaction technique that uses radioisotopes as probe nuclei[19]. These probe nuclei are added to the nanoparticles during nucleation and growth syntheses in extremely low quantities (fractions of ppm) acting as radioactive tracers sensing different regions inside the nanoparticles[20,21]. Moreover, local techniques based on hyperfine interactions have been applied to numerous nanoparticles and their results have been very important to understand the magnetic properties and local crystalline structure. Among them, we can mention the Mossbauer spectroscopy in Fe_3O_4, Fe_2O_3, FePt nanoparticles among others[18,22,23]. In addition, Nuclear Magnetic Resonance (NMR) and muon spin rotation have been used to study the magnetic and structural properties in different types of nanoparticles[24–26].

Cobalt monoxide (CoO) NPs have attracted much attention by the numerous technological applications directly associated with chemical, structural and magnetic properties. In the nanometric scale, the CoO can be crystallized in the rock-salt cubic phase (space group $Fm\bar{3}m$) or the hexagonal wurtzite type (space group $P63mc$)[28,29,35]. Anomalous magnetic behavior has been observed in rock-salt type CoO NPs, for example, a ferromagnetic ordering in CoO nanocrystals with size smaller than 10-20 nm. At first, this ferromagnetic behavior was attributed to a decompensation of spins on the surface of very small CoO nanoparticles indicating that the surface spins play a significant role as suggested by Néel and discussed in works of NiO and MnO[30–33]. However, in more recent reports the origin of ferromagnetic behavior at room temperature is still a matter of debate[34,35]. In contrast, it is well known that the CoO fcc bulk has an antiferromagnetic behavior with a well-established Neél temperature around 292 K. On the other hand, the physical properties of the hcp-wurtzite phase have been the subject of recent studies, where the antiferromagnetic ordering in NPs with size of 45 nm was observed around $T_N \sim$245 K[34].

In the work reported in this paper, the main purpose is the investigation of the local electronic and magnetic properties, to determine the magnetic phase transition and the possible existence of local distortions in CoO nanoparticles by measuring hyperfine interactions by PAC spectroscopy. Samples of CoO NPs were synthesized by a wet chemical route, the thermal decomposition, which offers several advantages such as the control and low dispersion of particle size and allows the possibility of incorporating radioactive tracers – in the present work, the ^{111}In nuclei - during the synthesis process. The hyperfine measurements were carried out in a wide range of temperatures in order to understand the structural and magnetic local proprieties. Additionally, the local properties were correlated with X-ray diffraction (XRD) and ZFC-FC magnetic measurements. The nanoparticles size and shape morphologies are described by high-resolution transmission electron microscopy (HRTEM). .

Results

TEM images of the samples S1 and S2 are displayed in Fig. 1 and show that S1 is composed by spherical-shape particles with average sizes distribution around 6.5 nm. On the other hand, S2 particles show a cuboid shape with an average size around 22 nm but with a non-uniform distribution.

High-resolution transmission electron microscopy (HRTEM) images of particle edge reveal the [111] and [200] orientations of CoO phase in S1 and S2 nanocrystals as displayed in Fig. 1c and d. Distinctive sets of fringes can be unambiguously identified in some particles with (111) and others with (200) orientation planes. The clear and single type of lattice fringes free from dislocations and stacking faults indicate a single-crystalline nature.

XRD patterns of S1 and S2 samples are displayed in Fig. S2 in the Electronic Supplementary Information (ESI) and for both samples the main peaks (111), (200), (220), (311), (222) and (400) of Bragg planes are consistent with fcc-CoO structure phase. A single phase for the as-prepared S1 sample is observed, which corresponds to the fcc structure of CoO with lattice parameter of 4.2665 Å. S2 sample presents two phases. The main phase (around 99 %) corresponds to the fcc structure with lattice parameter of 4.2676 Å. The minority phase (around 1 %) matches to the hcp structure of Co. This metallic phase is ascribed to be formed during the thermal treatment, which induces the oxide reduction[35,59]. The Scherrer equation was used in

order to obtain the crystallite average size, which are ∼7 nm for S1 and ∼20 nm for S2, both values totally agree with the TEM results as shown above.

Spin rotation spectra $R(t)$ of sample S2 measured by PAC at 10 K and at room temperature are displayed in Fig. 2. Spectrum taken at room temperature was fitted with a model considering that probe nuclei occupy two site fractions with pure electric quadrupole interaction. The major fraction (site A) with population $f_A = 65\%$, is characterized by a broadly distributed ($\delta_A = 80\%$) quadrupole frequency $\nu_{QA} = 62(4)$ MHz and asymmetry parameter $\eta = 0.35(2)$. Site A was ascribed to probe nuclei occupying the external layer of the nanoparticles where the reminiscent organic material covering the nanoparticles is present. A schematic drawing representing the layers of the particle is displayed in Fig. 2c. The minor fraction (site B) with population $f_B = 35\%$ presents a less distributed ($\delta_B = 30\%$) and small quadrupole frequency $\nu_{QB} = 11(2)$ MHz with asymmetry parameter $\eta_B = 0$. The small value of ν_Q and the fully symmetric site environment lead to the assignment of probe nuclei to substitutional cationic sites in a cubic structure, as expected for fcc-CoO. At room temperature, CoO is paramagnetic and, therefore, no dipole magnetic interactions are expected.

However, at 10 K, the magnetic interaction is present, and we have achieved an excellent fit of these spectra considering a model using two site fractions with combined interactions. The major fraction ($f_A = 65\%$), corresponding to probe nuclei at site A in the external layer of the particles, as described above, now is characterized by a quadrupole frequency $\nu_{QA} = 17(2)$ MHz with asymmetry parameter $\eta_A = 0$. plus a magnetic frequency $\nu_{MA} = 37.1(2)$ MHz which corresponds to a magnetic hyperfine field $B_{hf} = 16.1(2)$ T . This site fraction presents a high frequency distribution with $\delta_A = 40\%$ that was attributed to points of defects near to surface, such as oxygen vacancies. The presence of coating organic material at this external layer is not discarded.

On the other hand, at low temperatures, the site fraction B, with population $f_B = 35\%$, shows low frequency distribution attributed to substitutional position of nuclei probe. In addition, this site is characterized by a combined interaction of electric quadrupole with $\nu_Q B = 12(2)$ MHz, $\eta_B = 0$ and magnetic frequency $\nu_{MB} = 40.2(2)$ MHz with the angle between the directions of V_{zz} and B_{hf}, $\beta = 27^o$. As mentioned before, because the quadrupole frequency is very small, site B was assigned to probe nuclei at substitutional Co sites in the cubic structure of CoO. This assignment is reinforced by the observed magnetic frequency for site B, corresponding to a magnetic hyperfine field $B_{hf} = 17.1(2)$ T, which value totally agrees with 17.1(3) T reported by Rinneberg and Shirley[37] for the magnetic hyperfine field at ^{111}Cd nuclei in CoO. The mechanism of spin density transfer from Co ions to the s electrons of Cd occurs through the six oxygen nearest neighbors that octahedrally surround the Cd ion. This spin polarization from the Co atoms nearest neighbors is transferred by orbital overlap with the oxygen atoms but only those forming a linear Co^{+2}–O–Cd^{+2} bond with an angle of 180^o. Small differences in the B_{hf} values can be due to defects near Cd atoms or small distortions in the linear bond resulting in angles slightly different from 180^o at low temperature.

Figure 3 displays the spin-rotation spectra and the corresponding fast Fourier Transform (FFT) for different temperatures within a wide range. It is important to stress that PAC measurements on sample S2 were taken with increasing temperatures from 10 K to 670 K. All spectra taken in the 10–250 K range were fitted with the same two-site-fraction model described above used to fit the spectrum at 10 K: a major fraction corresponding to site A (external layer of NPs) and a minor fraction to site B (internal region of NPs). Results of the fit show that spectra from 250 K to 670 K present the site B with low-frequency ν_{QB}, which corresponds to probe nuclei in a crystalline cubic environment (any modulation in the spectrum has not been observed). The temperature dependence of ν_{QB} shows a step around 250 K with a reduction in its value and a subsequent slightly decrease when temperature increases, due to the thermal expansion of the lattice, whereas the asymmetry parameter $\eta_B = 0$ for all the temperature range. The abrupt change in ν_{QB} is related to known tetragonal distortion in CoO when the magnetic ordering is established[38]. The effect of this distortion is a contraction along the c axis with a possible deviation of the 3d radial function from a spherical distribution[38]. Therefore, the contraction along the c axis is expected to induce an increase in V_{zz} (and ν_Q), as it was experimentally observed and it is displayed in Fig. 3. It is noteworthy that previous PAC measurements of EFG in CoO using ^{111}Cd as probe nuclei could not detect the change at the ordering temperature[37,39].

The temperature behavior of probe nuclei at site A is puzzling. At low temperatures, ν_Q and η are similar to those of site B, though with a broader frequency distribution. At the ordering temperature and above, ν_Q and η increase intensively, indicating that the presence of oxygen vacancies near the surface have a strong influence on the local environment of cation sites. The population of probe nuclei at site A decreases deeply for temperatures above 500 K due to the crystallization of the region near the surface of particles.

In particular, the spectrum at 250 K shows a sharp decrease in the initial amplitude within a few nanoseconds (ns) indicating an interaction with relatively high frequency. This effect can be ascribed to a broad frequency distribution or to the onset of a magnetic interaction due to a strong disorder. Nevertheless, below 250 K a clear dipole magnetic contribution appears but with damped amplitude for all spectra.

Figure 4a displays the temperature dependence of B_{hf} for both A and B sites determined from the fit to PAC spectra measured at temperatures below 250 K in S2. Results show that B_{hf} of site A (corresponding to the major fraction) has a clear tendency to show a magnetic behavior with ordering temperature around 290 K as indicated by the solid curve that represents

the Brillouin function for $S = 5/2$ fitted to the experimental values. On the other hand, values of B_{hf} for site B show tendency to present a higher ordering temperature, which is estimated to be around 320 K. The antiferromagnetic ordering of small nanosystems of CoO with the Wurtzite-hexagonal structure (hcp-CoO phase) is $T_N \sim 245$ K[24,26]. Since the value of T_N observed for sample S2 is higher, it was not possible to discard the occurrence of this phase.

In turn, results from the temperature dependence of ZFC-FC magnetization with an applied field of 100 Oe (see Fig. 4b) for sample S1 show a large peak in the ZFC curve corresponding to a broad distribution of blocking temperatures with a maximum at $T_B \sim 250$ K. Because $T_B \propto K_{eff}V$, where K_{eff} is the magneto-crystalline anisotropy constant and V is the magnetic volume of the nanoparticles, one possible explanation for the broad distribution of T_B is the wide size distribution of the nanoparticle diameter as revealed by TEM image. On the other hand, because the total anisotropy is due core and surface contribution ($K_{eff} = K_{core} + K_{surface}$), a symmetry break at the surface can originate a strong contribution to K_{eff}. Other interesting characteristic on ZFC-FC curves is the behavior at low temperatures; our results show a pronounced increase of magnetization. As discussed above and shown by PAC results, small nanoparticles can present several types of defects on their surface, such as atomic vacancies, changes in the atomic coordination and amorphous phases, that may produce a magnetic disorder and contribute to the sharp increase at low temperatures as discussed by Qilin Dai *et al.*[34], Fontaíña-Troitiño *et al.*[28], and H. Shi and X. He[40].

Figure 4c displays the $M - H$ hysteresis curves for S1 sample measured at low temperatures. One can clearly observe a linear dependence of magnetization for all measured temperatures, characteristics of antiferromagnetic or paramagnetic behavior contribution. Fig. 4c also shows (see the inset) a small coercive field of about 27 Oe at 2 K. This coercive field is likely due to uncompensated spins on the particle's surface similar to those previously observed for CoO and NiO[30,41]. This magnetic behavior is in agreement with the PAC spectra which show a significant frequency distribution for all $R(t)$ spectra suggesting strong surface-disorder effects. Therefore, the results allow us to conclude that the NPs present a high degree of spins and crystal surface disorder and PAC measurements are able to detect it and quantify it through the site fraction determination. Moreover, the behavior of the temperature dependence of the hyperfine parameters is a strong evidence of the possible coupling between the magnetic and electrical properties.

After thermal annealing, the S2 sample was placed in a close-cycle refrigerator to carry out new PAC measurements at low temperatures. The spin rotation spectra were recorded starting from 10 K up to room temperature. All $R(t)$ spectra were fitted using a model considering that probe nuclei occupy two site fractions. For example, the spin rotation spectra at 10 K (see results in Fig. S3a in the ESI) was fitted using the following two fractions: the site B (major fraction), corresponding to probe nuclei located at the core of nanoparticle at substitutional cation sites, and site A (minor fraction) was attributed to the probe nuclei at a region near the nanoparticle surface (see Fig. S3b in ESI).

PAC spectra and their corresponding FFT for some temperatures within a wide range are shown in Fig.5. Differently from results obtained after synthesis for the same sample S2, it is interesting to note that now PAC spectra show well-defined magnetic frequencies with good resolution FFT peaks characterizing the two dipole magnetic interactions ascribed to site A and site B.

The well-defined frequencies in spin rotation spectra $R(t)$ is a signature of probe nuclei at a regular crystalline environment which can be attributed to substitutional cation sites in the crystalline lattice of NPs due to the increase in their size from 6.5 nm to 22 nm during annealing procedure. As shown in Fig. 1d and Fig.S2b of ESI, a large orientated nanocrystal was observed by TEM images after annealing in sample S2. This result indicates a kinetic grown mechanism enhanced by the heating rate as reported in previous works[30,35,42,43]. Specifically, the growth of CoO nanoparticles is dependent on two mechanisms: a) Co diffusion into the remained organic coating, into the lattice and intra lattice, and, principally, b) by coalescence and orientated attachment of CoO nanoparticles. It is noteworthy that, in the case of coalescence, there is no particular preference for the attachment whereas for the orientated attachment, there is the occurrence of a common crystallographic alignment[44]. In addition, during that heating rate up to 670 K, the crystal lattice relaxes producing kinetic diffusion of ^{111}In(^{111}Cd) probe nuclei into nanoparticles.

Differently for small nanoparticles (sample S1 and S2 after synthesis), the $R(t)$ spectra above 250 K clearly show magnetic dipole interaction up to the transition temperature T_N = 290 K. This temperature behavior is characteristic of fcc-CoO antiferromagnetic ordering. Therefore, we can conclude that the broad frequency distribution observed by PAC spectra that is assigned for surface effects in the small-size nanoparticles of S2 after synthesis was reduced after the annealing due to the increase in size and crystallinity of NPs. This effect was described by a study using PAC spectroscopy to track surface effects on the modulation of the spin rotation spectra reported by Effenberger *et al.* using ^{111}In (^{111}Cd) probe nuclei in Fe_3O_4 nanoparticles[20]. Additionally, an anomalous local behavior of the ν_Q around the magnetic transition temperature similar to that observed before annealing is also present (see Fig. 5b). The difference is that after annealing the population of site fractions ($\sim$80% for site B and $\sim$20% for site A) remains the same of those observed for 670 K during the annealing (see Fig. 3b). It was suggested that the temperature dependence of EFG tensors could give information on the onset of charge or orbital ordering and support the idea of local tetragonal distortion of oxygen coordination emerging below the magnetic transition temperature,

which can be correlated with short-range magnetic interactions[38]. Similarly to small particles (6.5 nm), the hyperfine data support the possible coupling between the magnetic and electrical properties below temperature transition (see Fig. 5b and 3b).

Figure 6 displays B_{hf} as a function of temperature and results of magnetization measurements for sample S2 after annealing. The behavior of B_{hf} as a function of temperature for both sites A and B is consistent with the CoO antiferromagnetic interactions with Néel temperature around T_N ~290 K, which characterizes the rock-salt antiferromagnetic structure. The magnetic dipole interaction at the lowest temperature for site A with site fraction population f_A = 20% is characterized by B_{hf} = 17.1 (2) T plus an electric quadrupole interaction with quadrupole frequency ν_Q = 5(1) MHz with asymmetry parameter η_B = 0. Above 250 K, ν_Q = ~60 MHz and η_B = 0.2, suggesting local distortion at the surface region. On the other hand, at site B with fraction population f_B = 80% a similar behavior for the magnetic dipole interaction was observed with B_{hf} = 17.3(2) with quadrupole frequency ν_Q = 19.5(3) MHz, η = 0 and angle between B_{hf} and the V_{zz} of $\beta = 30^o$. This quadrupole interaction may be associated with local distortions and the origin of the structural tetragonal deformation of CoO has been debated and attributed to the magnetostrictive effect of the spin-orbit coupling below the magnetic ordering temperature[45,46], whereas another work suggests that the origin is due to the Jahn-Teller distortion[47].

Our results show that the structural tetragonal distortion of the CoO_6 octahedra in CoO with a contraction along the c axis is noticeable by PAC measurements with ^{111}Cd probe nuclei with an expected increase in V_{zz} at temperatures below T_N. It is important to mention that the PAC technique is sensitive to local changes and has been applied to several studies such as perovskite types and multiferroic materials in which electronic distortions are predominant[48–51].

The occurrence of angle $\beta = 30^o$ between B_{hf} (along the magnetic moment direction) and V_{zz} was observed using other techniques such as neutron diffraction measurements in CoO single crystal where an angle of 27^o between the *c*-axis of the crystal and the magnetic moment at Co atoms has been reported[52,53]. For powder nanoparticles, the angles were between 59^o and 44^o below transition temperature[54]. A good example of PAC spectroscopy technique sensitivity to V_{zz} and B_{hf} angle occurrence has been noted in thin film surface regions studies such as: terrace, interfaces, incorporated-step and ultrafine films where the efg using ^{111}Cd can present in regions close to surface their values changed depending on the position.[55].

The ZFC-FC curves in Fig. 6b do not show any indication of temperature transition (T_N) and blocking temperature (T_B) until to 300 K. In contrast with the sharp increase in the ZFC-FC curves at low temperature observed for small nanoparticles (displayed in Fig. 4), the ZFC curve shows a decrease in M values at very low temperatures, whereas the FC curve remains practically unchanged below 50 K. This difference is probably a consequence of the thermal treatment that reduce the capping material, the presence of defects, internal void and strains. On the other hand, it was observed that the $M-H$ curve for sample S2 presents an *S*-like shape, a fingerprint of the ferromagnetic coupling, in the hysteresis cycle (see Fig. 6c). In addition, the behavior of the curve even for high fields does not show any tendency to saturate. This is an indication of the presence of strong competitions between ferromagnetic interactions and frustrated magnetic state interactions.

Since X-ray diffraction analysis also supported by hyperfine parameters has shown that the CoO NPs have the fcc crystal structure and, therefore, would order antiferromagnetically, what is the origin of the ferromagnetic behavior? In fact, the ferromagnetism at room temperature is a topic of intense discussion by the academic community and two positions are the most probable in the case of CoO ferromagnetism. In the first one the ferromagnetic behavior in room temperature has been attributed to "uncompensated" and "frustrated" surface moments on nanoparticle, this fact is a consequence of reduced surface coordination, called by the Néel theory[30–33,56]. Also, this uncompensated spin moment may be formed due to the presence of a thin Co2O3 layer on the surface of CoO, and the Coulomb repulsion, due to the charge transfer process of Co^{3+} to Co^{2+} at CoO/Co_3O_4 interface, has been suggested by Li *et al.* as the origin of the ferromagnetic behavior[57]. However, in our work we discard the presence of the thin layer of Co_2O_3 because its phase has shown temperature transition around 40 K and this fact was not observed by our magnetic measurements[28,58].

In the second position, the occurrence of ferromagnetism may be attributed to the presence of metallic cobalt contributions formed during the thermal treatment, as in the case studied in this paper due to the annealing in a helium atmosphere until 670 K. During the annealing, a diffusion mechanism of Co atoms may be involved allowing the occurrence of probable dilute Co clusters. In fact, the presence of low intensity peaks in the X-ray patterns as shown in Fig. 2c within the range of 2θ ~45^o-48^o corresponding to metallic hcp cobalt structure indicate the presence of metallic cobalt. Complementary, as previously reported, CoO phase may be reduced to metallic Co at high temperature in vacuum yielding Co/CoO interface in nanoparticles[42,59]. Therefore, the presence of metallic Co in sample S2 after annealing is likely to be associated with site A.

Another point is that even above room temperature (300 K), the S-like magnetic behavior is present with coercive field (H_c = 149 Oe) whereas at 10 K, H_c = 260 Oe, which is characteristic of the ferromagnetic contribution probably due to the presence of metallic cobalt. It is worth noting that the transition temperatures for both hcp and fcc metallic phases are approximately 680 K and 1030 K, respectively. On the other hand, we would like to emphasize that although an annealing process was carried out, core-shell nanostructures were not identified in transmission electron microscopy (TEM). Moreover, a striking feature of the core-shell structures is the presence of an exchange bias field[60] that was not observed in our $M-H$ results for both samples. Therefore, we believe that during annealing procedure, dilute small clusters of magnetic metallic Co were formed on the surface

or into CoO nanocrystals. The PAC spectroscopy is a high-sensitive local technique that requires the incorporation of probe nuclei into the crystalline lattice of the studied sample. PAC results of sample S2 only show hyperfine fields compatible with CoO, as described above, which strongly indicates an affinity of ^{111}Cd with fcc-CoO phase. The magnetic hyperfine fields for metallic cobalt were reported to be -16.4 T, -28.6 T, and -23.7 T, respectively for bcc, hcp, and fcc structures when using the ^{111}Cd nuclei probe[57], but these fields were not observed in this experiment. Reinforcing this conclusion, measurements in the metallic phases using PAC spectroscopy were only possible by introducing the parent nucleus by ion implantation methods[61]; because these metallic phases have a high degree of packing which makes it difficult to locate the probe nuclei inside the metal particles.

Discussion

As previously mentioned the magnetic transition temperature is a very important parameter for nanoparticles and often it is not clearly determined from magnetic techniques due to superposition of blocking temperature. PAC measurements with ^{111}Cd at Co sites determined the magnetic transition temperature for CoO NPs just after synthesis and after annealing at two site fractions ascribed to the core and surface of particles. In these NPs with different sizes it was possible to observe contributions from two magnetic dipole interactions that are predominant with temperature transition around 250 K and 290 K at 6.5 nm and 22 nm, respectively. It is worth noting that this low transition temperature around 250 K for 6 nm particles is due to the competition of interactions between the core and the surface of the CoO nanoparticles which would present a lack of compensation due to structural and magnetic disorder in the region near the surface which is evidenced below 250 K.

Moreover, a predominant fcc CoO structure with additional low intensity ($\sim$0.8 %) peaks, attributed to the presence of dilute metallic hcp Co clusters, was observed in the XRD pattern for the 20 nm NPs formed after annealing. PAC results show no magnetic dipole interactions above room temperature for this sample in agreement with paramagnetic interactions at fcc CoO structure. These facts allow us to conclude that the Cd^{+2} probe ion has a strong affinity with CoO rock-salt (fcc). Reinforcing this conclusion, measurements in the metallic phases using PAC spectroscopy were only possible by introducing the parent nucleus by ion implantation methods; because these metallic phases have a high degree of packing which makes it difficult to locate the probe nuclei inside the metal particles.

Finally, an anomalous temperature dependence behavior of electric hyperfine parameters were observed at temperatures around the magnetic ordering transition. The temperature dependence of the quadrupole frequency clearly indicates a crystalline distortion. Furthermore, it is suggested that the temperature dependence of EFG tensors can give information on the onset of charge or orbital ordering and support the idea of local distortion of oxygen coordination with short-range magnetic interactions in agreement with other reports. In conclusion, hyperfine interactions measured by PAC with ^{111}Cd as probe nuclei is a sensitive tool to locally characterize and investigate magnetic properties, formation of dilute impurity clusters and slight crystalline structural distortions.

Methods

^{111}Cd is one of the most used probe nuclei for PAC measurements due to optimal nuclear properties as well as due to the atomic properties of the radioactive ^{111}In parent nucleus. There are different routes to introduce radioactive nuclei as dilute impurities into matrices like nanoparticles, thin films or bulks. In the present work, radioactive ^{111}In nuclei were then introduced into samples during the CoO-NPs synthesis.

Synthesis of nanoparticles

Samples of CoO nanoparticles were synthesized by the thermal decomposition method described by Effenberger *et al.*[20]. In this synthesis, 2 mmol of Cobalt (II) acetylacetonate were dissolved in 20 ml of diphenyl ether, 4 mmol of oleylamine, 6 mmol of oleic acid and 10 mmol of 1,2-octanediol. A three-neck flask was used to mix and homogenize the reagents using an ultrasonic cleaner equipment. The flask was connected to a condenser and the mixture was heated at 258^{o}C for 2 h under nitrogen atmosphere. After cooling to room temperature, ethanol (proportion of 1:3) was added to the solution, and then the nanoparticles were precipitated and separated through centrifugation at 5000 RPM per 30 minutes. This last process was repeated three times until the liquid solution became clear, in order to remove the excess of organic material. The precipitate was dried under low pressure (about 1 kPa) per 24 h and a resulting powder was obtained. To perform PAC measurements a small volume of radioactive $^{111}InCl_3$ was added to the initial solution during the preparation of nanoparticle samples.

Characterization of nanoparticles

After the synthesis, the resulting powder sample was separated in two parts. One part, hereafter called sample S1, was used to check the structural and magnetic properties of the particles after the synthesis procedure. The second part, hereafter called sample S2, was placed in the sample holder of the He closed-cycle refrigerator device to be measured at different temperatures in

a range from 10 K to room temperature (RT) using the PAC spectrometer with four-BaF_2 detectors of the Hyperfine Interactions Laboratory in the "Instituto de Pesquisas Energeticas e Nucleares" (IPEN) in São Paulo, Brazil. These measurements were carried out to investigate the behavior of as-synthesized CoO nanoparticles at low temperatures. After measurements below RT, the sample S2 was sealed in a quartz tube under low pressure of argon (around 0.2 atm) and placed inside a small furnace to be measured in the PAC spectrometer while being annealed. This annealing followed by PAC measurements started at room temperature with subsequent steps with temperature being increased of 100 K after each one until reaching 670 K. Each step had a dwell time of 12 h during which the spin rotation spectra were acquired. After this annealing, the sample S2 were cooled down to RT and had PAC spectra taken at different temperatures in the range from 10 K to 300 K. These measurements were carried out to investigate the behavior of CoO nanoparticles at low temperatures after the annealing. The sample S2 was then stored until the activity was low enough to be considered as background radiation. The size and morphology of samples S1 and S2 were then checked by transmission electron microscopy (TEM) while the crystalline structure was analyzed by X-ray diffraction (XRD). The magnetic characterization of both samples S1 and S2 was performed by magnetization measurements with field cooling (FC) and zero field cooling (ZFC) in the temperature range from 2 K to 300 K as well as magnetization as a function of the applied field. Fig. S1 in the ESI presents a schematic sequence of measurements and annealing of both samples after synthesis. A brief description of the PAC technique as well as the main equations involving the hyperfine parameters are described below, further details of the technique can be found elsewhere[62].

Perturbed angular correlation technique: a brief overview

The method is based on the conservation of angular momentum between the spin direction of the intermediate level of a γ-emitter probe nucleus which emits two gamma radiations, γ_1 and γ_2 in cascade, and the direction of the γ_2 emission pattern. The hyperfine interaction consists of the coupling of the total angular momentum (J) of the electrons with the spin (I) of the nuclear intermediate level. When the probe nucleus is inserted into a material, the hyperfine interaction induces a time variation of this emission pattern and its measurement in a plane at different angles permits obtaining the components of the electric field gradient (EFG) tensor and/or the intensity of the magnetic hyperfine field (B_{hf}). Combined electric plus magnetic hyperfine interactions can also be measured. The number of radioactive nuclei necessary to perform experiments is generally less than 10^{12}, which in most cases represents a highly diluted concentration in the range between 0.01 and 1 ppm. This number of atoms is still enough to produce an observable modulation of the decay curve of the coincidence function obtained from the γ_1 and γ_2 simultaneous detection. The ratio of these functions measured with detectors at 90^o and 180^o is described by the so-called anisotropy ratio ($R(t)$) given by $R(t) = \sum_i A_{22} f_i G^i_{22}$. A fit to the $R(t)$ function, also usually referred as spin-rotation function, allows identifying multiple fractions (f_i) of probe atoms surrounding by different local environments in which these probes interact with the charge and spin density through hyperfine interactions given by respective perturbation functions ($G^i_{22}(t)$). A_{22} is the angular correlation coefficient, which for ^{111}In(^{111}Cd) is A_{22} = -0.18[63][37]. Because A_{22} is negative, the spin-rotation spectra for ^{111}Cd is displayed as $-R(t)$ with the y axis inverted.

For electric quadrupole interactions, the perturbation function is given by $G_{22} = S_{20} + \sum_{n=1}^{3} S_{2n}(\eta) cos(\omega_n t) exp(-\delta_n \omega_n t)$, with the transition frequencies ω_n being related to the quadrupole frequency $\nu_Q = (eQV_{zz})/h$ by $\omega_n = g_n(\eta)\nu_Q$, where Q is the nuclear electric quadrupole moment of the intermediate level of nuclear probe, and the exponential factor accounts for a Lorentzian distribution of relative width δ_n on the transition frequencies ω_n. The coefficients $g_n(\eta)$ and $S_{2n}(\eta)$ are functions of the asymmetry parameter $\eta = (V_{xx} - V_{yy})/V_{zz}$, where V_{kk}, with k = x,y,z, denotes the principal component of the electric field gradient (EFG) tensor. Since Q of the probe nucleus is well known, the experimental determination of $\nu_Q = eQV_{zz}/h$ allows the calculation of the major component (V_{zz}) of EFG as well as the measure of η provides information about the configuration of the electric field gradient in the crystallographic site where the probe nuclei are localized. The parameter η, with values limited to $0 < \eta < 1$, thus measures the deviation of the local charge distribution from axial symmetry due to local distortion of the crystallographic site. Hence, it is important to stress that η gives information on the local symmetry around the probe nucleus.

The perturbation function for a pure magnetic interaction is given by $G_{22}(t) = 0.2 + 0.4 \sum^{2}_{(n=1)} cos(n\omega_L t) exp(-\delta\omega_L t)$, where ω_L is the Larmor frequency and its experimental determination allows the calculation of the magnetic hyperfine field B_{hf} since $\omega_L = g\mu_N B_h f/\hbar$, where μ_N is the nuclear magneton and g is the nuclear g-factor. In combined electric quadrupole plus magnetic dipole interactions, the angle (β between directions of V_{zz} and B_{hf} can also be determined. Details regarding the experimental methodology, particularly PAC measurements on metal and oxides, can be found elsewhere[48,64–67]. Radioactive nuclei are added to samples to be measured by PAC through several methods. Ionic implantation and thermal diffusion are two usual methods[68,69]. Thermal diffusion, by its nature, requires samples to be heated at high temperature for long period. Ionic implantation usually needs a rapid thermal annealing at very high temperature for a short time to minimize the irradiation damage in the crystalline structure due to collisions with ions. Both methods are, therefore, not suitable for introduction of radioactive nuclei in nanoparticle samples, since high temperatures may modify the shape and size of particles. Additionally, ion implantation requires nanostructured systems with minimum sizes greater than one hundred nm, depending on the energy of the implanting ions otherwise the radioactive ions crosses the system without stopping inside it. ^{111}Cd yielded by the

electron-capture decay of ^{111}In is one of the most used probe in PAC technique due to the optimal nuclear properties of both the parent ^{111}In and the daughter ^{111}Cd as well as the electronic configuration of the Cd ion.

References

1. Heiligtag, F. J.; Niederberger, M. The fascinating world of nanoparticle research. *Materials Today* **16**, 262-271. https://doi.org/10.1016/j.mattod.2013.07.004 (2013).
2. Tarascon, J. M.; Armand, M. Issues and Challenges Facing Rechargeable Lithium Batteries. *Nature* **414**, 359-367. https://doi.org/10.1038/35104644 (2001).
3. Zeng, H.; Li, J.; Liu, J. P.; Wang, Z. L.; Sun, S. H. Exchange-Coupled Nanocomposite Magnets by Nanoparticle Self-Assembly. *Nature* **420**, 395-398. https://doi.org/10.1038/nature01208 (2002).
4. Willard, M. A.; Kurihara, L. K.; Carpenter, E. E.; Calvin, S.; Harris, V. G. Chemically Prepared Magnetic Nanoparticles. *Int. Mater. Rev.* **49**, 125-170. https://doi.org/10.1179/095066004225021882 (2004).
5. Raj, K.; Moskowitz, R. Commercial Applications of Ferrofluids. *J. Magn. Magn. Mater.* **85**, 233-245. https://doi.org/10.1016/0304-8853(90)90058-X (1990).
6. Yu, W.; Xie, H. A Review on Nanofluids: Preparation, Stability Mechanisms, and Applications. *J. Nanomaterials* **2012**, 435873. https://doi.org/10.1155/2012/435873 (2012).
7. Ganta, S.; Devalapally, H.; Shahiwala, A.; Amiji, M. A review of stimuli-responsive nanocarriers for drug and gene delivery, *J. Controlled Release* **126**, 187-204. https://doi.org/10.1016/j.jconrel.2007.12.017 (2008).
8. Franke, M. E.; Koplin, T. J.; Simon, U. Metal and Metal Oxide Nanoparticles in Chemiresistors: Does the Nanoscale Matter? *Small* **2**, 36-50. https://doi.org/10.1002/smll.200500261 (2006).
9. Keller, A. A.; Wang, H.; Zhou, D.; Lenihan, H. S.; Cherr, G.; Cardinale, B. J.; Miller, R.; Ji, Z. Stability and Aggregation of Metal Oxide Nanoparticles in Natural Aqueous Matrices. *Environ. Sci. Technol.* **44**, 1962-1967. https://doi.org/10.1021/es902987d (2010).
10. Laurent, S.; Forge, D.; Port, M.; Roch, A.; Robic, C.; Elst, L. V.; Muller, R. N. Magnetic Iron Oxide Nanoparticles: Synthesis, Stabilization, Vectorization, Physicochemical Characterizations, and Biological Applications. *Chem. Rev.* **108**, 2064-2110. https://doi.org/10.1021/cr068445e (2008).
11. Chen, H. M.; Peng, H.-C.; Liu, R.S.; Hu, S.F.; Jang, L.-Y. Local structural characterization of Au/Pt bimetallic nanoparticles. *Chem. Phys. Lett.* **420**, 484-488. https://doi.org/10.1016/j.cplett.2005.12.086 (2006).
12. Li, Y. H.; Liu, P. F.; Pan, L. F. ; Wang, H. F. ; Yang, Z. Z. ; Zheng, L. R. ; Hu, P.; Zhao, H. J. ; Gu, L.; Yang, H. G. Local atomic structure modulations activate metal oxide as electrocatalyst for hydrogen evolution in acidic water. *Nature Commun.* **6**, 8064. https://doi.org/10.1038/ncomms9064 (2015).
13. Bødker, F.; Mørup, S.; Linderoth, S. Surface effects in metallic iron nanoparticles. *Phys. Rev. Lett.* **72**, 282-285. https://doi.org/10.1103/PhysRevLett.72.282 (1994).
14. Mørup, S.; Hansen, M. F.; Frandsen, C. Magnetic interactions between nanoparticles, *Beilstein J. Nanotechnol.* **1**, 182–190. https://doi.org/10.3762/bjnano.1.22 (2010).
15. van der Zaag, P. J.; Ijiri, Y.; Borchers, J. A.; Feiner, L. F.; Wolf, R. M.; Gaines, J. M.; Erwin, R. W.; Verheijen, M. A. Difference between Blocking and Néel Temperatures in the Exchange Biased Fe_3O_4/CoO System. *Phys. Rev. Lett.* **84**, 6102-6105. https://doi.org/10.1103/PhysRevLett.84.6102 (2000).
16. Bedanta, S.; Kleemann, W.; Superparamagnetism. *J. Phys. D: Appl. Phys.* **42**, 013001. https://doi.org/10.1088/0022-3727/42/1/013001 (2008).
17. Kolhatkar, A. G.; Jamison, A. C.; Litvinov, D.; Willson, R. C.; Lee, T. R. Tuning the Magnetic Properties of Nanoparticles. *Int. J. Mol. Sci.* **14**. 5977-6009. https://doi.org/10.3390/ijms140815977 (2013).
18. Stahl, B.; Gajbhiye, N. S.; Wilde, G.; Kramer, D.; Ellrich, J.; Ghafari, M.; Hahn, H.; Gleiter, H.; Weissm´uller, J.; Beygzadeh, S.; Schlossmacher, P. Electronic and Magnetic Properties of Monodispersed FePt Nanoparticles. *Adv. Mater.* **14**, 24-27. https://doi.org/10.1002/1521-4095(20020104)14:1<24::AID-ADMA24>3.0.CO;2-O (2002).
19. Zacate, M. O.; Jaeger, H. Perturbed angular correlation spectroscopy – A tool for the study of defects and diffusion at the atomic scale. *Defect Diffus.Forum* **311**, 3-38. https://doi.org/10.4028/www.scientific.net/DDF.311.3 (2011).
20. Effenberger, F. B.; Carbonari, A. W.; Rossi, L. M. The influence of 1,2 alkanediol on the crystallinity of magnetite nanoparticles. *J. Magn. Magn. Mater.* **417**, 49–55. https://doi.org/10.1016/j.jmmm.2016.05.028 (2016).

21. Correa, B. S.; Costa, M. S.; Cabrera-Pasca, G. A.; Sena, C.; Pinto, R. H. H.; Silva, A. P. S.; Carvalho Jr, R. N.; Ishida, L.; Ramon, J. G. A.; Freitas, R. S.; Saiki, M.; Matos, I. T.; Correa, E. L.; Carbonari, A. W. High-saturation magnetization in small nanoparticles of Fe_3O_4 coated with natural oils. *J. Nanopart. Res.* **22**, 68. https://doi.org/10.1007/s11051-020-4761-5 (2020).

22. Hansen, M. F.; Koch, C. B.; Steen, M. Magnetic dynamics of weakly and strongly interacting hematite nanoparticles. *Phys. Rev. B.* **62**, 1124-1135. https://doi.org/10.1103/PhysRevB.62.1124 (2000).

23. Mørup, S.; Madsen, D. E.; Frandsen, C.; Bahl, C. R. H.; Hansen, M. F. Experimental and theoretical studies of nanoparticles of antiferromagnetic materials. *J. Phys.: Condens. Matter* **19**, 213202. https://doi.org/10.1088/0953-8984/19/21/213202 (2007).

24. Frandsen C.; Mørup S.; Spin Rotation in α-Fe_2O_3 Nanoparticles by Interparticle Interactions. *Phys. Rev. Lett.* **94**, 027202. https://doi.org/10.1103/PhysRevLett.94.027202 (2005).

25. Willis, A. L.; Turro, N. J.; O'Brien, S. Spectroscopic Characterization of the Surface of Iron Oxide Nanocrystals. *Chem. Mater.* **17**, 5970-5975. https://doi.org/10.1021/cm051370v (2005).

26. Marbella, L. E.; Millstone, J. E. NMR Techniques for Noble Metal Nanoparticles. *Chem. Mater.* **27**, 2721-2739. https://doi.org/10.1021/cm504809c (2015).

27. He, X.; Song, X.; Qiao, W.; Li, Z.; Zhang, X.; Yan, S.; Zhong, W.; Du, Y. Phase- and Size-Dependent Optical and Magnetic Properties of CoO Nanoparticles. *J. Phys. Chem. C.* **119**, 9550-9559. https://doi.org/10.1021/jp5127909 (2015).

28. Fontaíña-Troitiño, N.; Liébana-Viñas, S.; Rodríguez-González, B.; Li, Z.-A.; Spasova, M.; Farle, M.; Salgueiriño, V. Room-Temperature Ferromagnetism in Antiferromagnetic Cobalt Oxide Nanooctahedra. *Nano Lett.* **14**, 640-647. https://doi.org/10.1021/nl4038533 (2014).

29. Lu, A.; Chen, Y.; Zeng, D.; Li, M.; Xie, Q.; Zhang, X.; Peng, D.-L. Shape-related optical and catalytic properties of wurtzite-type CoO nanoplates and nanorods. *Nanotechnology* **25**, 035707. https://doi.org/10.1088/0957-4484/25/3/035707 (2014).

30. Jagodič, M.; Jagličič, Z.; Jelen, A.; Lee, J. B.; Kim, Y. M.; Kim, H. J.; Dolinšek, J. Surface-spin magnetism of antiferromagnetic NiO in nanoparticle and bulk morphology. *J. Phys.: Condens. Matter* **21**, 215302. https://doi.org/10.1088/0953-8984/21/21/215302 (2009).

31. Bahl, C. R. H.; Lefmann, K.; Theil Kuhn, L.; Christensen, N. B.; Vazquez, H.; Mørup, S. Spin dynamics in weakly and strongly interacting NiO nanoparticles. *J. Phys.: Condens. Matter* **18**, 11203. https://doi.org/10.1088/0953-8984/18/49/013 (2006).

32. Morales, M. A.; Skomski, R.; Fritz, S.; Shelburne, G.; Shield, J. E.; Yin, M.; O'Brien, S.; Leslie-Pelecky, D. L. Surface anisotropy and magnetic freezing of MnO nanoparticles. *Phys. Rev. B* **75**, 134423. https://doi.org/10.1103/PhysRevB.75.134423 (2007).

33. Pishko, V. V.; Gnatchenko, S. L.; Tsapenko, V. V.; Kodama, R. H.; Makhlouf, S. A. Temperature dependence of magnetic resonance in NiO nanoparticles, *J. Appl. Phys.* **93**, 7382-7384. https://doi.org/10.1063/1.1558253 (2003).

34. Dai, Q.; Tang, J. The optical and magnetic properties of CoO and Co nanocrystals prepared by a facile technique. *Nanoscale*, **5**, 7512–7519. https://doi.org/10.1039/C3NR01971C (2013).

35. He, X.; Li, Z.; Zhang, X.; Qiao, W.; Song, X.; Yan, S.; Zhong, W.; Du, Y. Effects of Ar/H2 annealing on the microstructure and magnetic properties of CoO nanoparticles. *RSC Adv.* **5**, 69948-69954. https://doi.org/10.1039/C5RA09723A (2015).

36. Yang, G.; Gao, D.; Shi, Z.; Zhang, Z.; Zhang, J.; Zhang, J.; Xue, D. Room Temperature Ferromagnetism in Vacuum-Annealed CoO Nanospheres. *J. Phys. Chem. C* **114**, 21989-21993. https://doi.org/10.1021/jp106818p (2010).

37. Rinneberg, H. H.; Shirley, D. A. Supertransferred hyperfine interaction: Perturbed angular correlation of ^{111}Cd in antiferromagnetic NiO, CoO, and MnO. *Phys. Rev. B* **13**, 2138-2144. https://doi.org/10.1103/PhysRevB.13.2138 (1976).

38. Roth, W. L. Magnetic Structures of MnO, FeO, CoO, and NiO. *Phys. Rev.* **110**, 1333-1341. https://doi.org/10.1103/PhysRev.110.1333 (1958).

39. Inglot, Z.; Wegner, D.; Lieb, K.P. Hyperfine interaction of ^{111}Cd in antiferromagnetic cobalt oxide. *Hyperfine Interact.* **50**, 785–790. https://doi.org/10.1007/BF02407723 (1989).

40. Shi, H.; He, X. Large-scale synthesis and magnetic properties of cubic CoO nanoparticles. *J. Phys. Chem. Solids* **73**, 646-650. https://doi.org/10.1016/j.jpcs.2012.01.001 (2012).

41. Ghosh, M.; Sampathkumaran, E.V.; Rao, C.N.R. Synthesis and magnetic properties of CoO nanoparticles. *Chem. Mater.* **17**, 2348-2352. https://doi.org/10.1021/cm0478475 (2005).

42. López Antón, R.; González, J. A.; Andrés, J. P.; Canales-Vázquez, J.; De Toro, J. A.; Riveiro, J. M. High-vacuum annealing reduction of Co/Co Nanoparticles. *Nanotechnology* **25**, 105702. https://doi.org/10.1088/0957-4484/25/10/105702 (2014).

43. Gonzalez, J. A.; Andres, J. P.; De Toro, J. A.; Muniz, P.; Munoz, T.; Crisan, O.; Binns, C.; Riveiro, J. M. Co–CoO nanoparticles prepared by reactive gas phase aggregation. *J. Nanopart. Res.* **11**, 2105. https://doi.org/10.1007/s11051-008-9576-8 (2009).

44. Thanh, N. T. K.; Maclean, N.; Mahiddine, S. Mechanisms of nucleation and growth of nanoparticles in solution. *Chem. Rev.* **114**, 7610–7630. https://doi.org/10.1021/cr400544s (2014).

45. Jauch, W.; Reehuis, M.; Bleif, H. J.; Kubanek, F.; Pattison, P. Crystallographic symmetry and magnetic structure of CoO. *Phys. Rev. B* **64**, 052102. https://doi.org/10.1103/PhysRevB.64.052102 (2001).

46. Sarte, P. M.; Songvilay, M.; Pachoud, E.; Ewings, R. A.; Frost, C. D.; Prabhakaran, D.; Hong, K. H.; Browne, A. J.; Yamani, Z.; Attfield, J. P.; Rodriguez, E. E.; Wilson, S. D.; Stock, C. Spin-orbit excitons in CoO. *Phys. Rev. B* **100**, 075143. https://doi.org/10.1103/PhysRevB.100.075143 (2019).

47. Ding, Y.; Ren, Y.; Chow, P.; Zhang, J.; Vogel, S. C.; Winkler, B.; Xu, J.; Zhao, Y.; Mao, H.-K. Pressure-induced long-range magnetic ordering in cobalt oxide, *Phys. Rev. B* **74**, 144101. https://doi.org/10.1103/PhysRevB.74.144101 (2006).

48. Dogra, R.; Junqueira, A. C.; Saxena, R. N.; Carbonari, A. W.; Mestnik-Filho, J.; Moralles, M. Hyperfine interaction measurements in $LaCrO_3$ and $LaFeO_3$ perovskites using perturbed angular correlation spectroscopy. *Phys. Rev. B* **63**, 224104. https://doi.org/10.1103/PhysRevB.63.224104 (2001).

49. Lopes, A. M. L.; Araújo, J. P.; Ramasco, J. J.; Amaral, V. S.; Suryanarayanan, R.; Correia, J. G. Percolative transition on ferromagnetic insulator manganites: Uncorrelated to correlated polaron clusters. *Phys. Rev. B* **73**, 100408(R). https://doi.org/10.1103/PhysRevB.73.100408 (2006).

50. Ramirez, F. E. N.; Cabrera-Pasca, G. A.; Mestnik-Filho, J.; Carbonari, A. W.; Souza, J. A. Magnetic and transport properties assisted by local distortions in Bi2Mn4O10 and $Bi_2Fe_4O_9$ multiferroic compounds. *J. Alloys Compd.* **651**, 405-413. https://doi.org/10.1016/j.jallcom.2015.08.165 (2015).

51. Cabrera-Pasca, G. A.; Bosch-Santos, B.; Burmova, A.; Correa, E. L.; Carbonari, A. W. Effect of the magnetic impurity on the charge diffusion in highly dilute Ce doped $LaMnO_3$. *AIP Advances* **10**, 015223. https://doi.org/10.1063/1.5130429 (2020).

52. van Laar, B. Multi-Spin-Axis Structure for CoO. *Phys. Rev.* **138**, 584-587. https://doi.org/10.1103/PhysRev.138.A584 (1965).

53. Herrmann-Ronzaud, D.; Burlet, P.; Rossat-Mignod, J. Equivalent type-II magnetic structures: CoO, a collinear antiferromagnet. *J. Phys. C: Solid State Phys.* **11**, 2123-2137. https://doi.org/10.1088/0022-3719/11/10/023 (1978).

54. Silva, N. J. O.; Millán, A.; Palacio, F.; Martins, M.; Trindade, T.; Puente-Orench, I.; Campo, J. Remanent magnetization in CoO antiferromagnetic nanoparticles. *Phys. Rev. B* **82**, 094433. https://doi.org/10.1103/PhysRevB.82.094433 (2010).

55. Potzger, K.; Weber, A.; Zeitz, W.-D.; Bertschat, H. H.; Deicher, M. Magnetic response of isolated Cd impurities on ferromagnetic Ni surfaces and Ni-Pd interfaces: Access to ordered structures of polarized impurities with ultrahigh density. *Phys. Rev. B* 72, 054435. https://doi.org/10.1103/PhysRevB.72.054435 (2005).

56. Néel, L. in Low Temperature Physics. Dewitt, C.; Dreyfus, B.; deGennes, P.D., Eds., Gordon and Beach, New York, p 413. (1962).

57. Li, Z.-A.; Fontaíña-Troitiño, N.; Kovacs, A.; Liébana-Viñas S.; Spasova, M.; Dunin-Borkowski, R. E.; M´uller, M.; Doennig, D.; Pentcheva, R.; Farle, M.; Salgueiriño, V. Electrostatic Doping as a Source for Robust Ferromagnetism at the Interface Between Antiferromagnetic Cobalt Oxides. *Sci. Rep.* **5**, 7997. https://doi.org/10.1038/srep07997 (2015).

58. Thota, S.; Singh, S. Nature of magnetic ordering in cobalt-based spinels. In Magnetic Spinels – Synthesis, Properties and Applications. Seehra, M.S. Ed., InTech, Rijeka, p 04. (2017).

59. Yang, G.; Gao, D.; Shi, Z.; Zhang, Z.; Zhang, J.; Zhang, J.; Xue, D. Room Temperature Ferromagnetism in Vacuum-Annealed CoO Nanospheres. *J. Phys. Chem. C* **114**, 21989–21993. https://doi.org/10.1021/jp106818p (2010).

60. Feygenson, M.; Yiu, Y.; Kou, A.; Kim, K.-S.; Aronson, M. C. Controlling the exchange bias field in Co core/CoO shell nanoparticles. *Phys. Rev. B* **81**, 195445. https://doi.org/10.1103/PhysRevB.81.195445 (2010).

61. Swinnen, B.; Dekoster, J.; Langouche, G.; Rots, M. Magnetic hyperfine field on ^{111}Cd in metastable bcc cobalt. *Phys. Rev. B* **52**, 5962-5966. https://doi.org/10.1103/PhysRevB.52.5962 (1995).

62. Schatz, G.; Weidinger, A. *Nuclear Condensed Matter Physics: Nuclear Methods and Applications* (John Wiley and Sons: Chichester, UK, 1996).

63. Rinneberg, H. H. Application of perturbed angular correlation to chemistry and related areas of solid state physics. *At. Energy Rev.* **17**, 477-595. (1979).

64. Carbonari, A. W.; Mestnik-Filho, J.; Saxena, R. N. Impurities in magnetic materials studied by PAC spectroscopy. *Defect Diffus. Forum* **311**, 39-61. https://doi.org/10.4028/www.scientific.net/DDF.311.39 (2011).

65. Cabrera-Pasca, G. A.; Carbonari, A. W.; Saxena, R. N.; Bosch-Santos, B.; Coaquira, J. A. H. Magnetic hyperfine field at highly diluted Ce impurities in the antiferromagnetic compound $GdRh_2Si_2$ studied by perturbed gamma-gamma angular correlation spectroscopy. *J. Alloys Compd.* **515**, 44-48. https://doi.org/10.1016/j.jallcom.2011.10.077 (2012).

66. Mercurio, M. E.; Carbonari, A. W.; Cordeiro, M. R.; Saxena, R. N.; D'Agostino, L. Z. Local investigation of hyperfine interactions in pure and Co-doped ZnO. *J. Magn. Magn. Mater.* **322**, 1195-1197. https://doi.org/10.1016/j.jmmm.2009.06.051 (2010).

67. Correa, E. L.; Bosch-Santos, B.; Cavalcante, F. H. M.; Correa, B. S.; Freitas, R. S.; Carbonari, A. W.; Potiens, M. P. A. Properties of Gd_2O_3 nanoparticles studied by hyperfine interactions and magnetization measurements. *AIP Advances* **6**, 056112. https://doi.org/10.1063/1.4943601300 (2016).

68. Cristiano, F. Ion Implantation-Induced extended defects: structural investigations and impact on Ultra-Shallow Junction properties. Micro and nanotechnologies/Microelectronics. Université Paul Sabatier - Toulouse III, Rapport LAAS N° 13526 https://tel.archives-ouvertes.fr/tel-00919958 (2013).

69. Li, W. Q.; Xiao, X. H.; Stepanov, A. L.; Dai, Z. G.; Wu, W.; Cai, G. X.; Ren, F.; Jiang, C. Z. The ion implantation-induced properties of one-dimensional nanomaterials. *Nanoscale Res. Lett.* **8**, 175. https://doi.org/10.1186/1556-276X-8-1753 (2013).

Acknowledgements (not compulsory)

Financial support of this study was partially provided by the Conselho Nacional de Desenvolvimento Científico e Tecnológico (CNPq, grants number 473477/2013-0, 304627/2017-8, 430060/2018–1) and Fundação de Amparo á Pesquisa do Estado de São Paulo (FAPESP, grants number 2015/16191-5, 2017/50332-0, 2019/15620-0).

Author contributions statement

G.A.C.-P. and A.W.C. conceived and headed this study. R.V.S., C.S.C., and F.B.E. synthesized the samples and performed the X-ray diffraction measurements. R.S.F Performed the magnetic measurements and discussed them together with G.A.C.-P. and L.O. performed the Transmission Electron Microscopy measurements and the images were analyzed together with R.V.S.. B.B.-S., L.F.D.P., B.S.C., A.B., and A.W.C. performed the measurements and analysis of Perturbed Angular Correlation. G.A.C.-P., R.V.S., A.B., and A.W.C. wrote the manuscript. All authors reviewed the manuscript.

Competing interests

The authors declare no competing interests.

Additional information

Correspondence and requests for materials should be addressed to A.W.C.

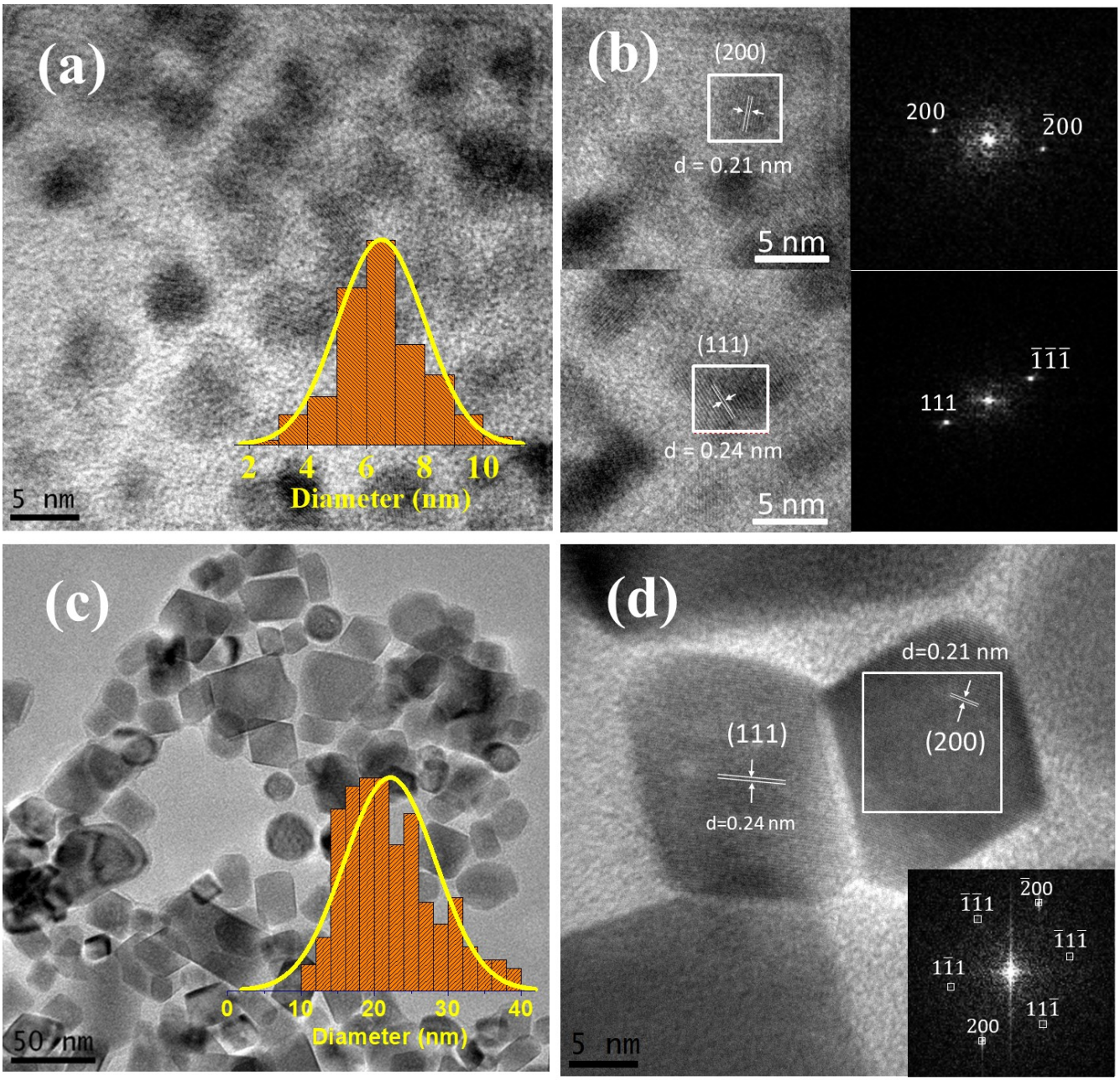

Figure 1. TEM images of CoO samples S1 (a) and S2 (c). The insets in (a) and (c) display the size distribution of particles. High-resolution (HRTEM) images of S1 (b) and S2 (d) revealing the regular arrangement of lattice fringes. The corresponding fast Fourier transform (FFT) of images are displayed in the insets in (b) and (d) and show the spacing of 0.24 nm and 0.21 nm at [111] and [200] orientations of CoO phase, respectively.

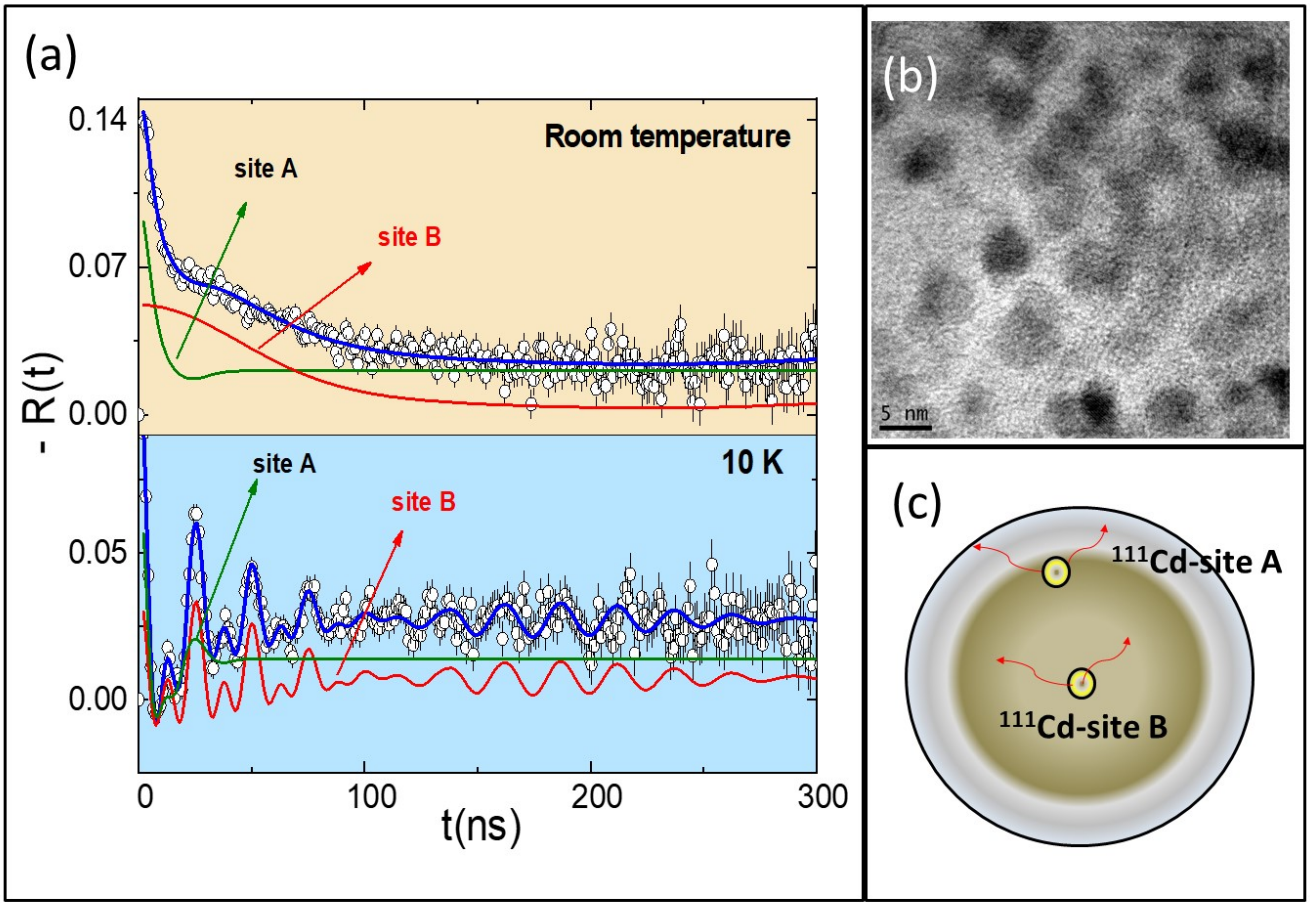

Figure 2. (a) Spin rotation spectra measured with ^{111}Cd in S2 sample at room temperature (top) and 10 K (bottom). (b) TEM image for sample S1. (c) Schematic drawing of the spherical particle displaying the positions of ^{111}Cd probe nuclei (represented by small yellow spheres).

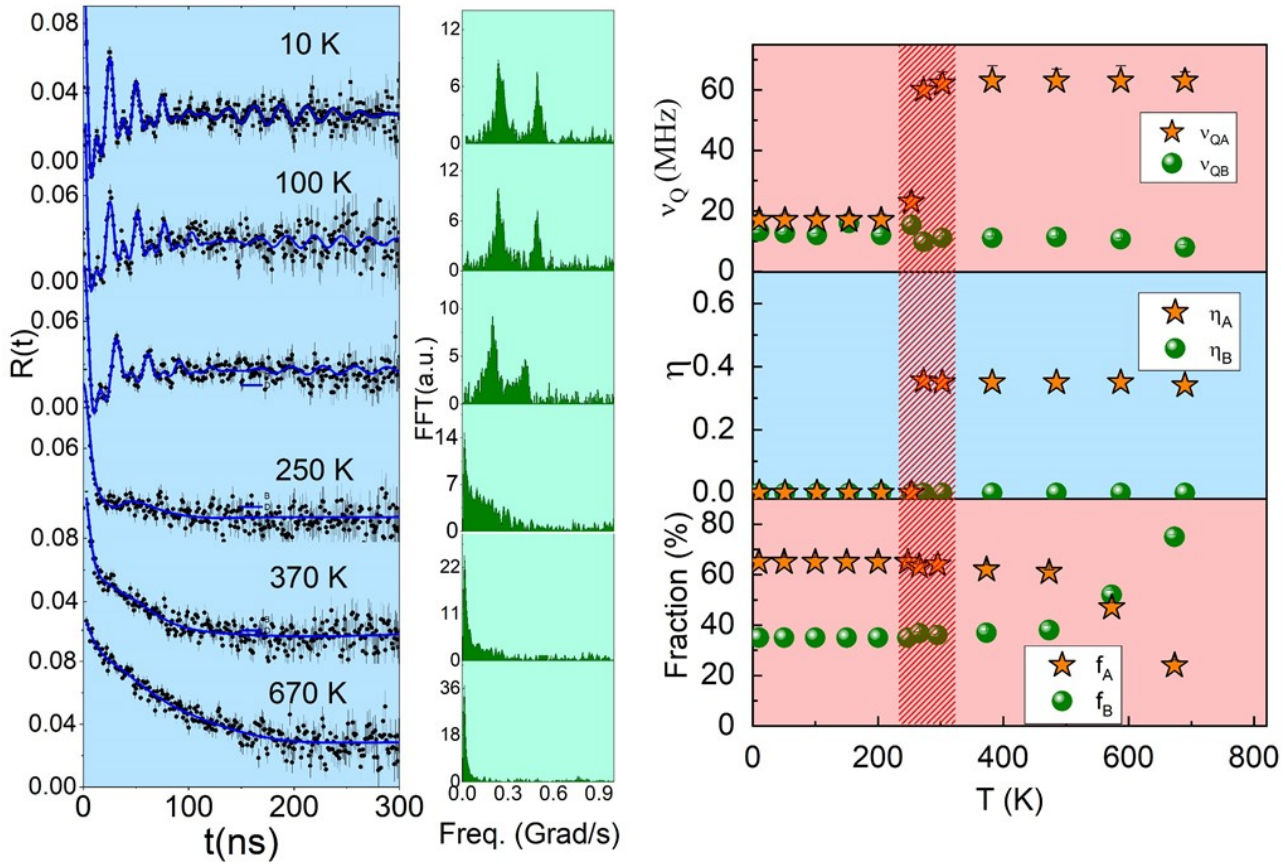

Figure 3. (a) PAC spectra and corresponding fast Fourier transform (FFT) measured with ^{111}Cd in sample S2 at different temperatures. Continuous lines represent the fit of theoretical functions to experimental data. Note that above 250 K no modulation of PAC spectra was observed. (b) Temperature dependence of the quadrupole coupling frequency (ν_Q), asymmetry parameter (η) and site fractions occupied by ^{111}Cd probes. Arrow lines are guide to the eye indicating the sequence of temperature.

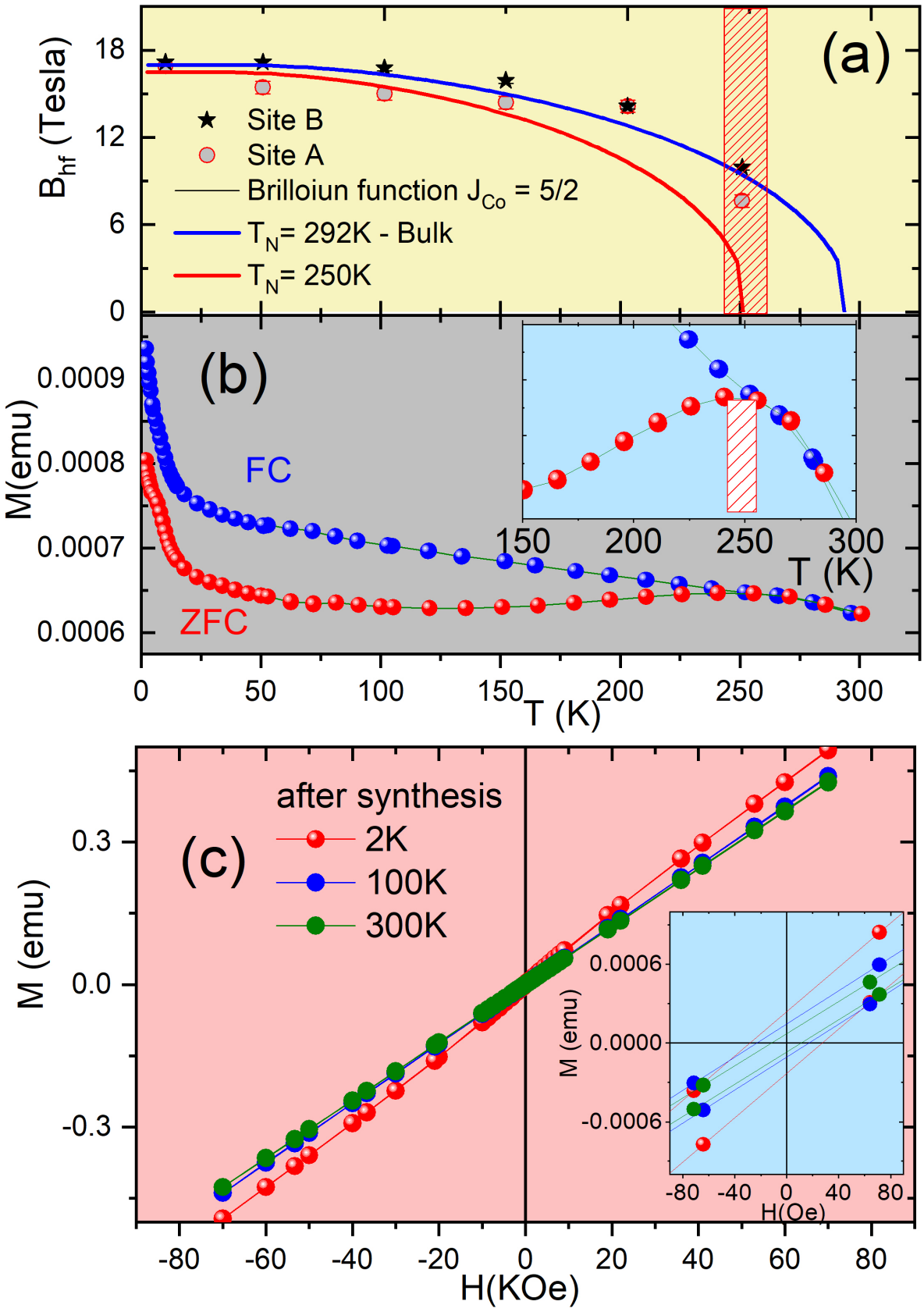

Figure 4. (a) Temperature dependence of B_{hf} at sites A and B measured with ^{111}Cd for sample S2 up to room temperature. The solid curves represent the Brillouin function for spin 5/2. The inset shows the maximum of the ZFC curve. (b) $M \times T$ curves and (c) $M - H$ curves for sample S1. The inset in (c) shows the coercive field.

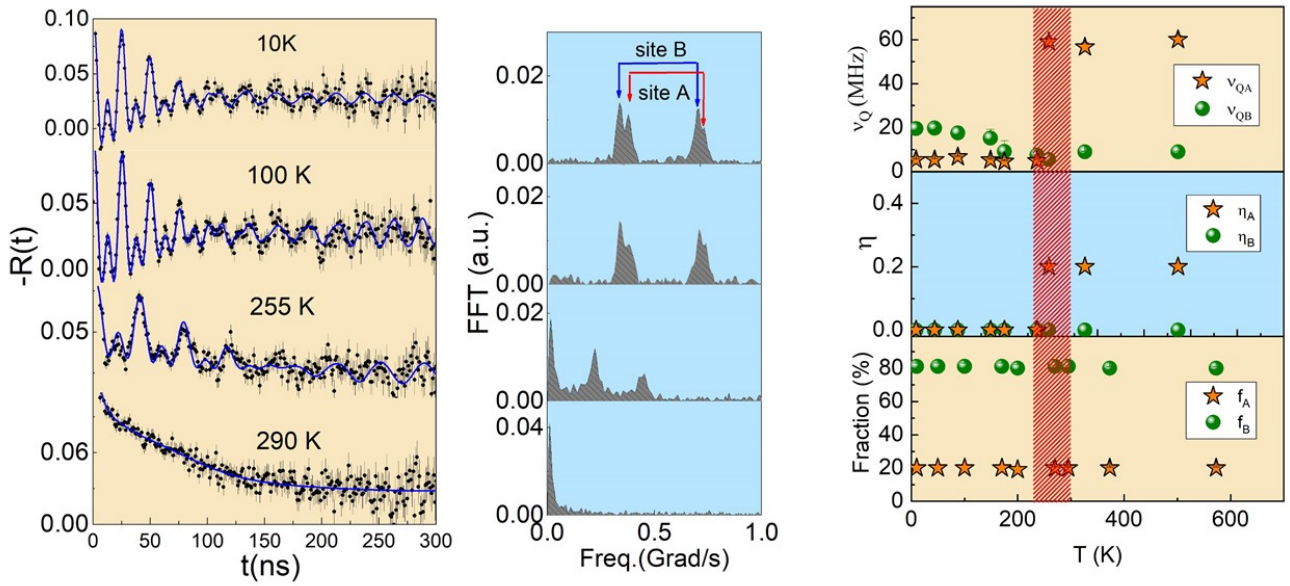

Figure 5. (a) Spin Rotation spectra measured with ^{111}Cd in S2 sample of CoO after annealing (left) and respective Fast Fourier Transforms (right). The continuous lines represent the fit of theoretical functions to experimental data. (b) Temperature dependence of the quadrupole coupling frequency (ν_Q), asymmetry parameter (η), and site fractions occupied by ^{111}Cd probes.

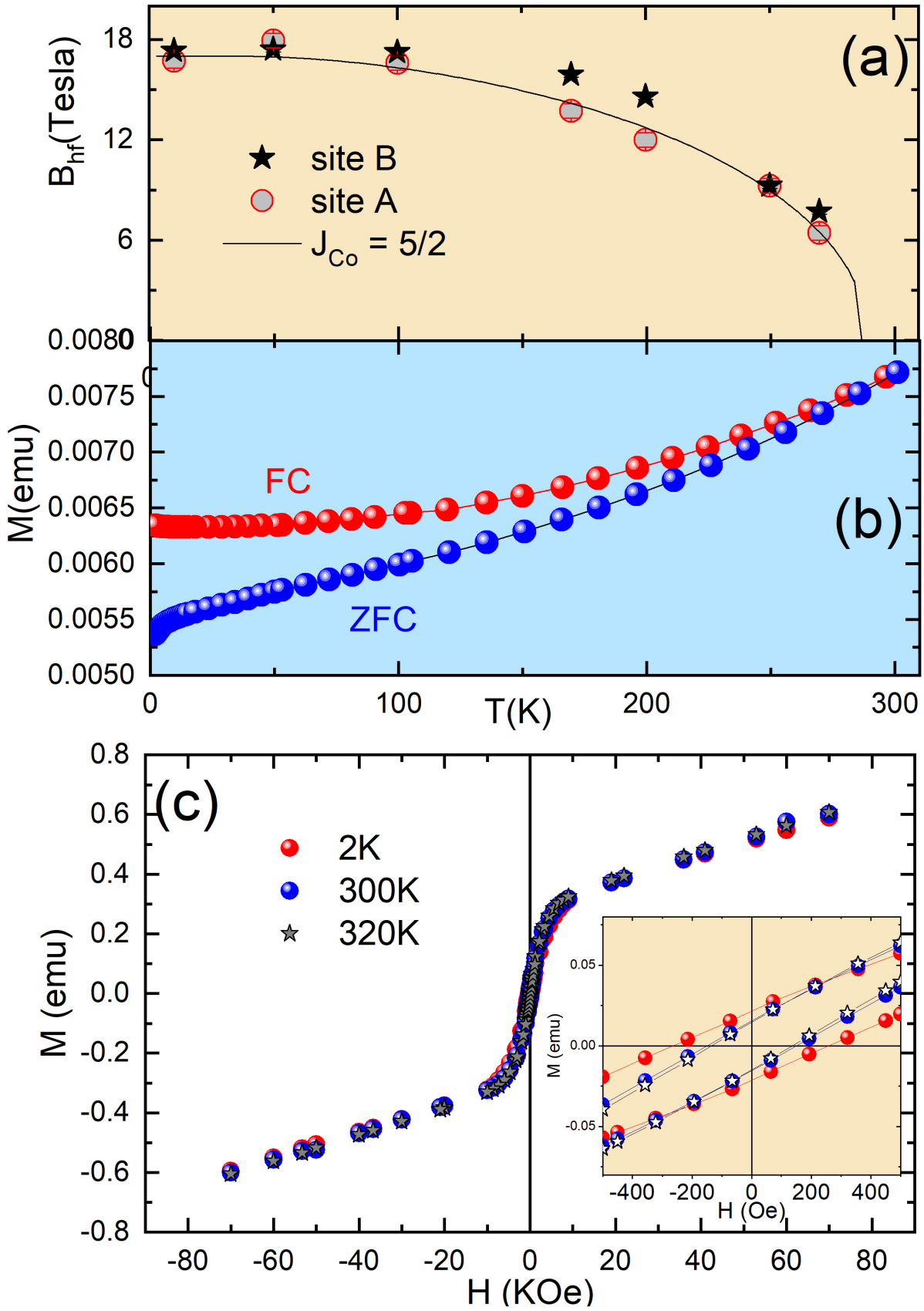

Figure 6. (a) Temperature dependence of B_{hf} measured with ^{111}Cd for sample up to room temperature. (b) $M \times T$ curves and (c) $M - H$ curves for sample S2 after annealing. The inset in (c) shows the coercive field.

Supplementary Files

This is a list of supplementary files associated with this preprint. Click to download.

- SupplementaryInformationpdf.pdf